Fabrication of low-cost Pt-free counter electrode for dye-sensitized solar cell and asymmetric supercapacitor electrode material based on rGO/$CoFe_2O_4$ nanocomposites for a viewpoint of energy conversion and storage devices

M. MANIKANDAN[1,2], V. ANTO FERADRICK SAMSON[1], E. MANIKANDAN[1,2,*], K. A. KARTHIGEYAN[3,*]

[1]*Centre for Advanced Materials and Innovative Technologies, Vellore Institute of Technology, Chennai 600127, India*
[2]*School of Electronics Engineering, Vellore Institute of Technology, Chennai 600127, India*
[3]*Department of ECE, Vel Tech Rangarajan Dr. Sagunthala R&D Institute of Science and Technology, Chennai, Tamilnadu, India*

The significant production of dye-sensitized solar cells (DSSCs) relies on the development of economical counter electrode (CE) equipment among superior electrocatalytic and electrochemical activity. Here, rGO/$CoFe_2O_4$ (rCoF) nanocomposites have been effectively created by one-pot hydrothermal technique and serve as counter electrodes for DSSCs. The loosely bound cobalt ferrite (CoF) nanoparticles were scattered on together faces of reduced graphene oxide (rGO) indicating a multilayer structure developing a free channel for particle diffusion. Correspondingly, the structural changes and the electrocatalytic features of rCoF nanocomposites were examined. The rCoF-50 CE demonstrated remarkable catalytic activity by speed up the reduction of triiodide ions in DSSCs due to its peculiar structural property and favourable chemical compositions. The DSSC assembled with rCoF-50 CE exhibits excellent power conversion efficiency (PCE) of 9.05%, that is larger than to facilitate of DSSC assembled among Pt (8.5%) and rCoF-25 (7.6%) CEs. This CE is also examined as an electrode for supercapacitors. Therefore, the device reaches a high specified capacity of 388.7 Fg^{-1} at 1 Ag^{-1}, and maintains 90.5% of capacity retention gone 2000 cycle at a current density of 3 Ag^{-1}, which clearly explains its capability for energy storage. The exceptional capacities behaviour and photovoltaic performances of rCoF-50 CE integrated with solar energy conversion and storage shows promising anticipation for innumerable extensive uses.

(Received April 9, 2024; accepted April 15, 2025)

Keywords: rGO/$CoFe_2O_4$, DSSCs, Asymmetric supercapacitor: photo storage devices

1. Introduction

Energy generation and energy storage are two main challenges faced globally and have attracted immense scientific attention for the past few decades [1]. The gradual rise of earth's temperature, and environmental challenges including fossil fuels exhaustion, have engrossed more and more consideration to various clean energy technologies such as hydrogen, photovoltaic, wind, geothermal, tidal power, etc. Among these, photovoltaic in specific has prompted a world-wide interest due to its plentiful supply, numerous distributions, green and sustainable energy conversion, and low costs [2]. Photovoltaics (PV) and large-scale power plants be the primary preferences to bloom in the mind while considering solar power and it should be accepted that such large-scale functions accompany its techno-economic glitches [3,4]. A supercapacitor is a new type of energy storage device that possesses special qualities such as long cycle life, high energy density, low discharge rate, fast charging, and a higher power density compared to traditional batteries. The active materials in electrochemical energy storage devices are crucial for controlling the potential range. Desirable qualities for an electrode material used in supercapacitors include good reversibility, fast kinetics, exceptional specific capacitance, high stability, long cycle life, affordability, and environmental friendliness. Electric double-layer capacitors (EDLCs) and pseudo capacitors are the two main types of supercapacitors, distinguished by their energy storage mechanisms [5-9]. Consequently, the application of solar energy with supercapacitor integration can be seen as the progress of a totally solar powered small-scale transportable and wearable electronic device, despite of its small density of energy and flashing environment of solar irradiation. Thus, "photo-super capacitors" (PSC) refer to the incorporation of supercapacitors among a light gathering method into a lone compressed component. [10]. An ideal PSC is projected to be constructed of low-cost components. It should be in such a way that it is upgradable to meet the required necessity and easy to fabricate. These require multiple solar cell technologies for "charging" and super-capacitors for the "storage" portion [11]. According to the

available literature on PSCs, it is important to note that not all solar cells can be adapted for conversion into PSCs. For a solar cell to function effectively as part of a PSC, it must possess specific properties and meet certain criteria. Among them, DSSCs were put in technical study for along with a decade since its low price, easy manufacture, high power conversion efficiency (PCE) and clean energy applications. The incorporation of DSSCs with a supercapacitor increases the conversion efficiency by surpassing electron recombination and provides a huge flow of electron for storage in the reservoir of the supercapacitor. Generally, Dye sensitized solar cells have several parts, such as a photo anode containing of light-absorbing dye molecules at speed on a semiconductor material, a dye sensitizer, redox couple electrolyte, and counter electrode. Among them, counter electrode executes an electrically conductive function by transferring photo generated electrons from the external circuit to the redox couple and catalysing a redox reaction (I^-/I_3^-) to regenerate electrons for the dye molecules. Platinum (Pt) loaded on a conductive substrate (FTO) is normally use as a CE suitable to its admirable electro catalytic activity which results in the collection of electrons from the outer circuit and functioning as a catalyst in the reduction reaction of the redox electrolyte. Hence, the shortage of Pt, due to its high price, and low chemical stability of iodide species has stop the practical applications in DSSCs [12-15]. So, it is of high importance to pursue the development of new types of efficient counter electrodes with high electrical conductivity and higher reduction rates of redox reaction. Up to date, several reports of electro catalytic materials has been explored to replace platinum CE, such as conducting polymers, carbon materials, inorganic compounds, and other composites. Among them, rGO, MWCNTs, sulphides, carbides, nitrates, and oxides material are used as counter electrodes to return Pt because of their rather low-priced, effortless preparation, good electrical conductivity and excellent electrocatalytic activity. Still, the conversion effectiveness and electrochemical strength are at rest lower than Pt CE suitable to several drawbacks such as, limited catalytic surface area, less electron transfers between the materials in the film and insufficient compatibility of polar triiodide electrolyte [16-17]. So, this is being addressed by researchers that carbonaceous supported binary or ternary metal oxide composite materials were synthesized to develop the conductivity as glowing as the electro catalytic motion to achieve superior device performance. Feng du et.al. reported that the composite SnO_2@rGO counter electrode obtained a power conversion effectiveness of 6.78%, which was superior than to facilitate SnO_2 nanoparticles (4.88%), and graphene sheets only (3.171%) as CEs and this worth is secure with the aim of Pt CE (7.22%) [18]. likewise, Kuangwei Xiong et.al. reported $La_{0.65}Sr_{0.35}MnO_3$@rGO nanocomposite, which was employed as a counter electrode and yielded a PCE of 6.57%, which was superior with the aim of of perfect LSMO CE (5.35%) or rGO CE (4.93%), respectively [19]. Vignesh Murugadoss et.al. reported cobalt nickel selenide/graphene nanocomposite with different ratios employed as counter electrode. Among them, DSSC cell with the $Co_{0.5}Ni_{0.5}Se/GN_{0.50}$ counter electrode brought PCE of 9.42%, which was superior to DSSC cell with $Co_{0.5}Ni_{0.5}Se$ (7.59%) and Pt (7.68%) counter electrodes [20]. Likewise, Yanfang wang et.al. synthesized S-rGO/MoS_2 nanocomposite counter electrode, which attained a PCE of (6.96 %) which was very close with the aim of Pt CE (7.35 %) [21]. this enrichment is owing to the company of rGO, which intensifies the electro catalytic activity and conductivity. In addition to carbonaceous hold-up counter electrodes, some scientists have created DSSCs using binary or ternary transition metal nanocomposites and have achieved superior performance. For example, Juan Xia et.al. reported metal selenide $M_{0.85}$ Se (M = Co & Ni) as the counter electrode in a bifacial dye-sensitized solar cell, $Co_{0.85}$ Se yielded the PCE of 8.33% and 4.79% in forward and behind irradiations, which was higher than the forward and behind efficiency of 7.44% and 4.05% for Pt and 7.23% and 4.16% for $Ni_{0.85}$ Se CEs. Likewise, $CoSe_2$-NC@$CoeFeSe_2$ and CoS_2-NC@$CoeFeS_2$ yolk-shell nanopolyhedrons prepared by Jiahui Yang et.al. achieved a PCE of 9.61 and 9.18%, correspondingly, which be greater to those of Pt (8.15%). Qing-song Jiang et.al. reported Co_9S_8 / rGO Nanocrystals showed excellent photovoltaic performance with a PCE of 7.31 %, which was comparable with DSSCs fabricated with Pt (6.51%) counter electrodes [22-24]. Taking a clue from these results, for the search of Pt-free, and low cost-efficient counter electrode material, spinel type mixed metal oxides MFe_2O_4 (M=Ni, Co, Zn, and Mn) coated between graphene sheets were observed as a CE material for DSSCs due to their chemical properties, small price, elevated strength beside corrosions, connections among metal ions providing more active sites, which improves the electrocatalytic activity of CEs. Altaf et al. Fabricated ZnO Nanoflowers and Nanowires for photo-supercapacitor, Both NW and NF-based PSCs had very similar dark Coulombic efficiency (CE%); under UV light, the CE% of NW PSC increased three times, while the CE% of NF PSC increased 1.7 times [25]. ZnO nanorods grown on FTO using BMIM-BF_4 electrolyte shows retention of 76.3% and 86.5% upto 6000 cycles in dark and UV illumination [26]. Under the specified light intensity, the V_2O_5||AC AS) with an FTO-based photo-assisted charging device achieved an areal capacity of 112 mC cm^{-2}. In contrast, when tested using the conventional method without light irradiation, the device only achieved an areal capacity of 45 mC cm^{-2} at the same current density. Furthermore, under light irradiation, the asymmetric FTO device demonstrated impressive performance, delivering a high specific energy density of 9.8 Wh kg^{-1} and a specific power density of 29 W kg^{-1}. [27]. ZnO:$ZnMn_2O_4$ electrode displays an areal capacitance of 4.45 mF/cm^2 under dark condition, notably the capacitance increases to 9.90 mF/cm^2 under light condition [28]. Based on this, we in situ rGO/$CoFe_2O_4$ (rCoF) nanocomposite by hydrothermal treatment with different reduced graphene oxide ratios and hence, employed counter electrode material in DSSCs. Furthermore, we have been working on the same electrode for supercapacitor applications for energy storage devices. Henceforth, it is supposed that the current work resolve

some ideas on rGO/$CoFe_2O_4$ (rCoF) nanocomposite for the usage of solar cells in combination with supercapacitors.

2. Experimental section

Initially, Natural graphite powder was used to synthesise graphene oxide (GO) and reduced graphene oxide (rGO) by a modified Hummer's technique [29]. The rGO/$CoFe_2O_4$ (rCoF) nanocomposite was making via one-pot hydrothermal approach. In brief, 25, 50, 75, and 100 mg of rGO was distributed into 40 mL of deionized water and ultrasonicated for 30 min separately to attain a uniform solution. Consequently, a 1:2 ratio of Cobalt nitrate hexahydrate and Iron nitrate monahydrate was added to 40 mL of distilled water. The reaction mixtures were then stirred continuously at an ambient room temperature. The above metal salt mixture was added dropwise to the dispersed rGO solution to make a homogeneous solution. To this mixture, an aqueous solution of NaOH (2 M) was added dropwise to regulate the PH range up to 10. Then the combined product was subsequently poured into a 150 mL of Stainless-steel autoclave and autogenously pressured for 10 hrs at 180° C. Finally, the resulting black-coloured products were gathered and then purified by washing several times with ultrapure water and ethanol. The obtained slurry-type samples were further dry at 60° C in a vacuum oven for 24 hrs, and the products was coded as rCoF-50 and rCoF-25. From the aforementioned procedures, the $CoFe_2O_4$ (CoF) synthesis route were followed without the incorporation of reduced Graphene Oxide. The schematic representation of rCoF nanocomposite was illustrated in Fig. 1.

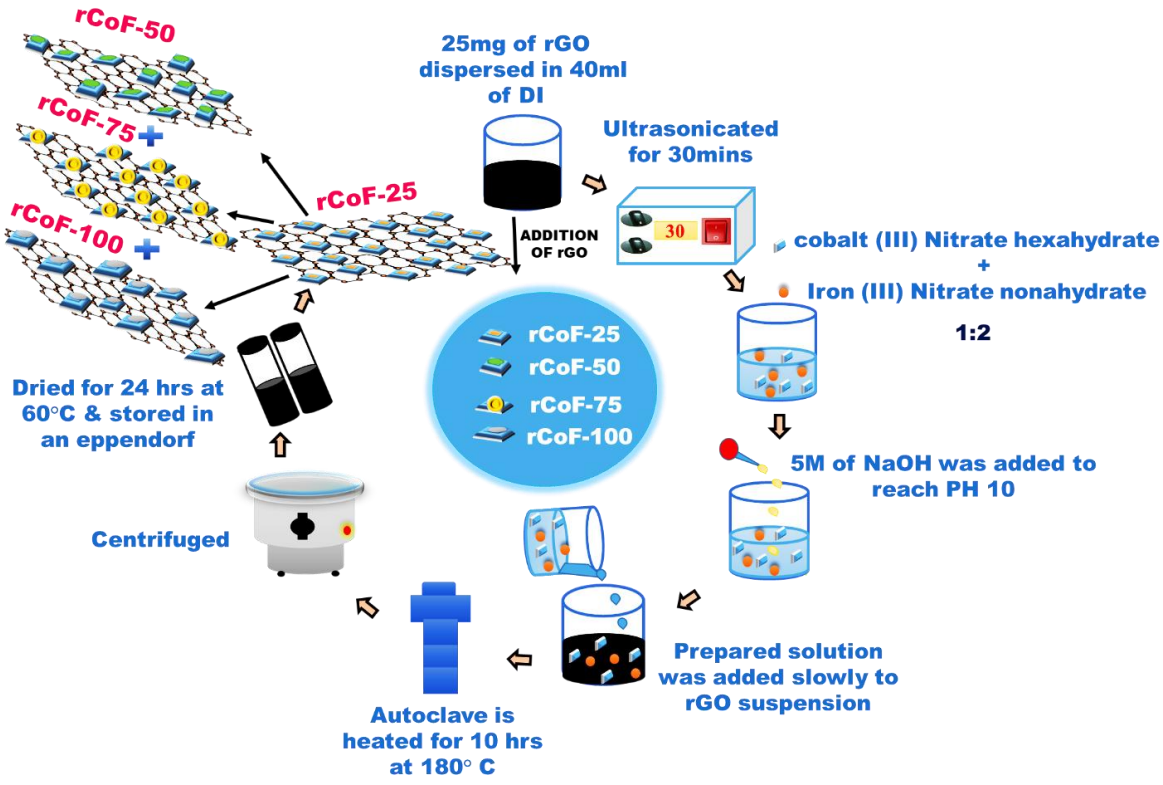

Fig. 1. The concise schematics of rCoF nanocomposites (colour online)

2.1. Electrode making and DSSC cell making

In order to construct rGO, CoF, rCoF-25 and rCoF-50 CE, each test was thoroughly grounded in a motor before being combined with polyvinylidene fluoride (PVDF), and the mixture was then dispersed in a N-Methylpyrrolidone solution (NMP) solution to make a homogeneous black slurry paste. The resultant sticky paste was subsequently coated on a clear FTO substrate using a conventional expert cutting edge approach, by a contact area of 1.5 cm^2. At the same time, the H_2PtCl_6 isopropanol solution was dropped-coated on to FTO substrates in order to prepare the pt CE, which was further heated to 400°C for 30 mins. Later than normal cool to ambient temperature, the CE was suitable for together photovoltaic and electrochemical investigations. To fabricate DSSCs, commercialize P25 TiO_2 fine particles was use as the photoanode material. The TiO_2 paste was apply to FTO glass substrates by the doctor blade procedure, covering an active area of 1.5 cm^2. The coated electrodes were calcined at 450°C for 30 minutes. The prepared photoanodes were then immersed in a 3 mM solution of N719 dye for 24 hours under dark conditions and subsequently dried at 60°C. After dye sensitization, the photoanodes were rinsed with ethanol to remove any loosely attached dye molecules.A liquid electrolyte consisting of iodide/triiodide (I_3^-/I^-) redox couple was prepared by dissolving 0.05 M potassium iodide in acetonitrile. The photoanode and counter electrode were

assembled, and the redox electrolyte was injected through a small opening in the counter electrode to complete the DSSC assembly and activate it for operation.

2.2. Characterization and measurements

Powder X-ray diffraction (XRD) analysis with Rigaku, D/MAX-2500/PC using Cu Kα (40 kV, 100 mA) was use to examine the formation of phase and crystal arrangement of the synthesized materials. High resolution-transmission electron microscope measurements were performed using HR-TEM ((JEM-2100). In adding, the existence of chemical constituents was considered by X-ray photoelectron spectroscopy (XPS, Thermo Scientific Co.) with monochromatic Al Kα radiation. The specific surface area (SSA) and pore size distribution of the powder be examined by the Tristar-3000 surface area analyzer. The electrochemical property of the as-synthesised material be analyzed by a three-electrode configuration, which consists of reference electrode as Ag/AgCl (3 M KCl), a Pt sheet as a counter electrode and the prepared samples rGO, Pt, CoF, rCoF-25, and rCoF-50 CEs as a working electrode, which was assessed in a potential series of 0 to 0.8 V at a sweep rate of 50 mV s^{-1}. The liquid electrolyte consisted of 0.5 M potassium iodide (KI) and 0.05 M iodine (I_2) dissolved in acetonitrile. Tafel polarization profiles for symmetrical cells made of two identical electrodes were evidence on the same workstation. Electrochemical impedance spectroscopy (EIS) measurements of the symmetric cells were performed at zero bias potential with amplitude of 10 mV, spanning a frequency range from 0.1 Hz to 100 kHz. The photovoltaic (J-V) performance of the device was evaluated at room temperature with a Keithley 2400 high-current source meter. A 500 W xenon lamp with AM 1.5G illumination simulated sunlight for the measurements. For supercapacitor applications, the electrochemical behavior of the prepared material was studied in a two-electrode configuration using a Biologic VSP workstation. Cyclic voltammetry (CV), galvanostatic charge-discharge (GCD), and EIS studies were conducted in a 1 M NaOH aqueous electrolyte.

The following formulas were used to compute the PCE and FF:[29]

$$\text{Efficiency (\%)} = \frac{J_{sc} * V_{oc} * FF}{P_{in}} \quad (1)$$

$$\text{Fill Factor} = \frac{J_{mp} * V_{mp}}{J_{sc} * V_{oc}} \quad (2)$$

Here, the J_{mp} - density of current and V_{mp} - voltage at the most power point

3. Results and discussion

3.1. X-ray diffraction (XRD)

X-ray Diffraction analysis is employed to resolve the phase clarity and structural characteristics of resultant as-analyzed powders. Fig. 2 (a and b) shows the phase structures of GO, rGO and compositions of CoF, rCoF-25 and rCoF-50. The typical peak around 9.8° corresponds to the plane (001) specify the victorious synthesis of GO from graphite powder. Following the chemical reduction process, the removal of oxygen-containing functional groups was confirmed by the appearance of a slight peak at 24.4°, corresponding to the (002) plane. This observation indicates the successful transformation of GO into rGO [30]. The diffracted peaks of CoF at 31.1°, 36.7°, 38.4°, 44.6°, 55.4°, 59.1°, 65.0°, 68.3° are certified to the (111), (220), (311), (222), (400), (422), (511), (440), and (531) crystal planes of CoF, matching very well with the stated values (JCPDS card No. 00- 012-0041) which suggests the fine quality of the nanoparticles [31]. Moreover, in the composite structure, the diffraction peaks of graphene were not found in both samples, which might be credited to their small diffraction intensity and the guarding of the graphene peaks by the strong diffraction peaks of CoF. As a result of this phenomenon, the graphene (002) plane might not have existed. Furthermore, in the rCoF composite structure, the CoF acted as a space between rGO and stacking keys and provided an increase in accessible surface area, which serves as a foundation for electrochemical in situ measurements. As the amount of rGO is increased from 75 to 100 mg, the structural phase of the powders becomes noisier and has additional peaks compared to those prepared with 25 and 50 mg. Based on these considerations, further exploration is conducted only through rGO, CoF, rCoF-25, and rCoF-50 nanocomposites. According to the Scherer equation, the crystallite size of CoF, rCoF-25, and rCoF-50 nanoparticles is estimated based on the XRD results [32]. The obtained crystallite sizes for CoF, rCoF-25 and rCoF-50 nanoparticles are 24.2, 17.1, and 14.3 nm respectively.

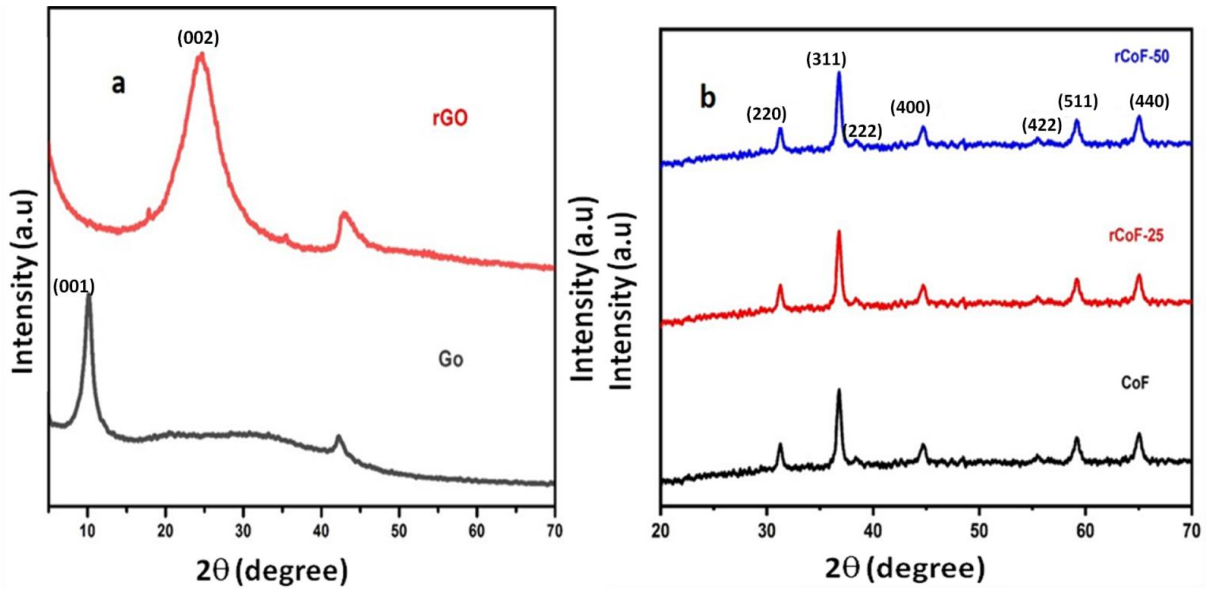

Fig. 2. XRD pattern of (a) GO and rGO (b) CoF, rCoF-25 and rCoF-50 (colour online)

3.2. High resolution-transmission electron microscopy (HR-TEM)

The surface morphologies and microstructures of the as-prepared samples are analyzed by HR-TEM. Fig. 3 (a and b) reveals the HR-TEM images and SAED pattern of rGO. HR-TEM images of CoF nanoparticles exhibit cubic size morphology are given in Fig. 3(c), the. As displayed in Fig.3 (e), CoF nanoparticles were homogeneously adhered to the outer surface of rGO sheets in the composite structures. It is evident that CoF nanoparticles are loosely packed and dispersed on together edges of rGO sheets, forming a multilayer structure, which may serve as an open channel for element dispersal.

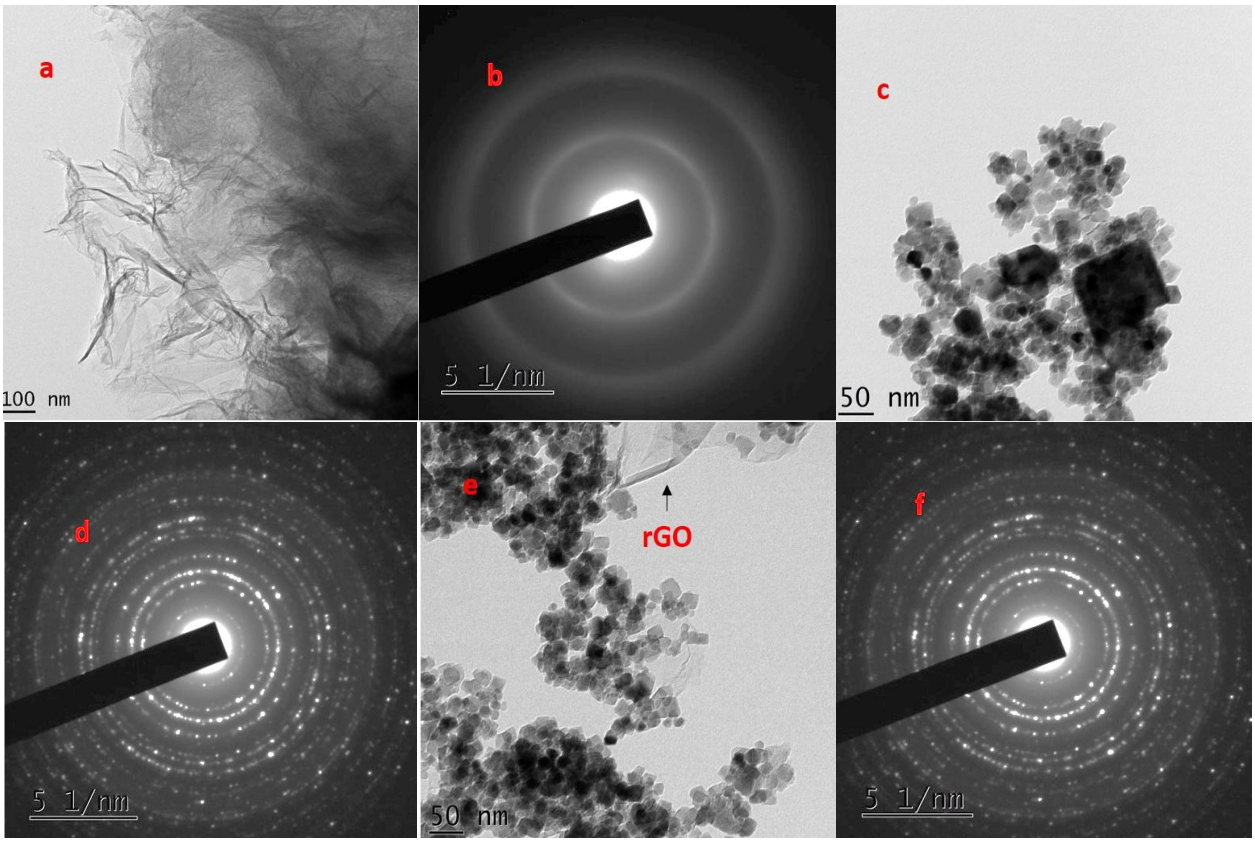

Fig. 3. rGO, CoF and rCoF-50 (a, c & e) HR-TEM images (b, d & f) SAED pattern (colour online)

Additionally, it appears to have a porous structure, providing more easily reached freedom for ion replace among electrode and electrolyte. Moreover, this type of composite structure can facilitate the utilisation of active materials, leading to high electrochemical performance [33-34]. The SAED pattern of reduced graphene oxide was illustrated in Fig.3 (b) confirming the reduced graphene oxide's amorphous nature. The SAED patterns of CoF and rCoF-50 nanoparticles are depicted in Fig.3 (d and f). The rings that were detected fit up well with the lattice planes of (220), (311), (222), (400), (422), (511), and (440), indicating that the as-synthesized samples are highly crystalline. Additionally, it also implies that the CoF crystal structure remains unchanged. From HR-TEM study, the particle sizes were evaluated to be 28.44, 22.8, and 17.71 nm for CoF, rCoF-25, and rCoF-50, respectively. This fine-sized particle is beneficial for electrolyte dispersion in the electrochemical environment [29]. The size of the particle is acquired from HR-TEM results is well-concordant with XRD findings.

3.3. X-ray photoelectron spectroscopy (XPS)

In instruct to prove the elemental composition, chemical valence state, bonding nature, and orbital distribution, results were examined through X-ray photoelectron spectroscopy (XPS). The survey spectrum of the rCoF composite was presented in Fig. 4 (a). The occurrence of atomic orbitals such as Co2p, Fe2p, O1s, and C1s with high resolution is revealed in Fig. 4 (b–e) respectively. As exposed in Fig. 4 (b), for the Co2p spectrum, the two primary peaks placed at 780.37 and 795.8 eV are recognized to the binding energies of $Co2p_{1/2}$ and $Co2p_{3/2}$, respectively. Moreover, two shake-up peaks at 803.44 eV corresponds to $Co2p_{1/2}$ and 787.32 eV associated with $Co2p_{3/2}$, points out the existence of Co^{2+} oxidation states in the rCoF nanocomposite [35].

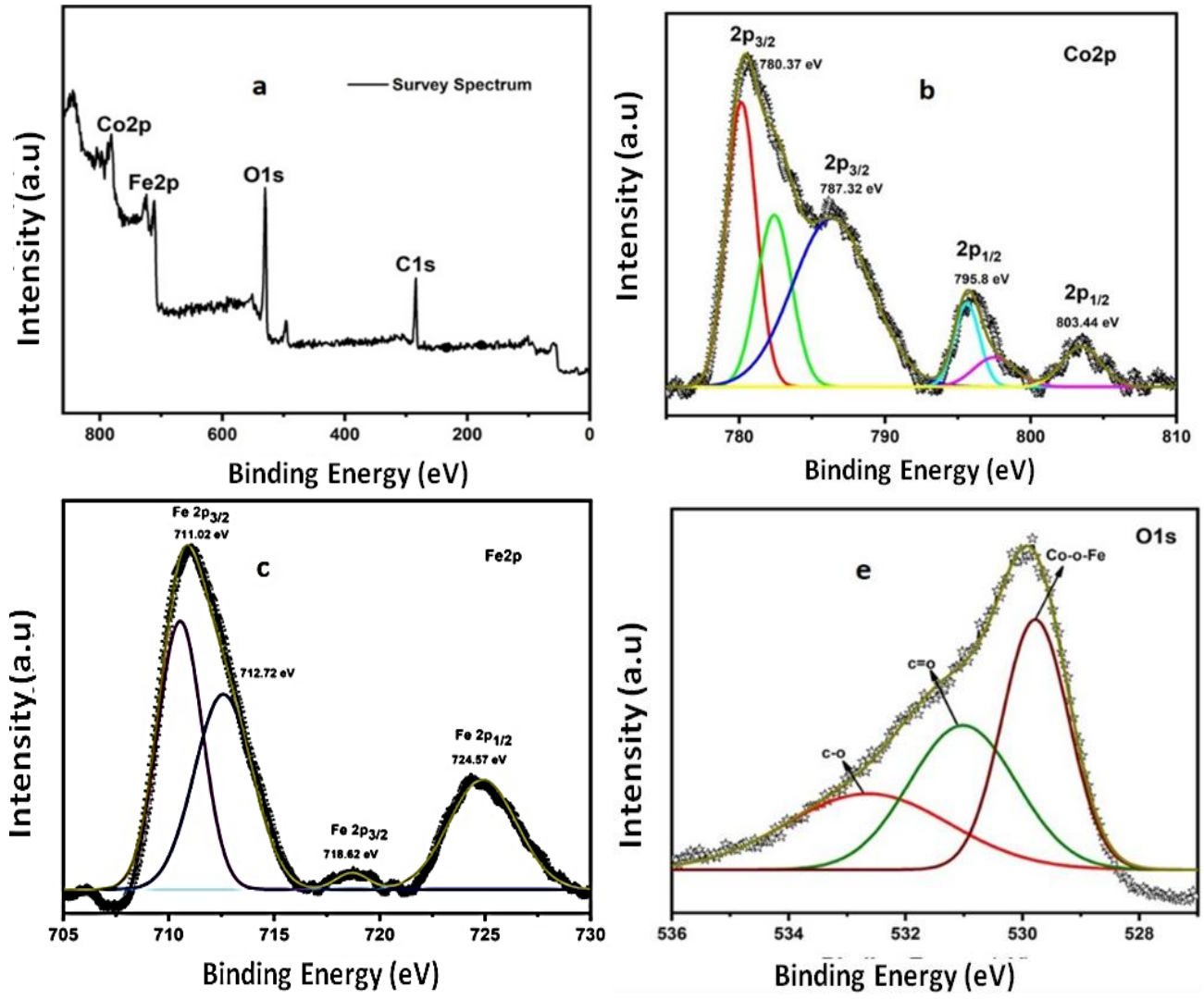

Fig. 4. (a) XPS survey spectrum, (b) Co2p, (c) Fe2p, (d) C1s spectrum and (e) O1s (colour online)

In Fig. 4 (c), the peaks at 711.02 and 724.57 eV were assign to $Fe2p_{3/2}$ and $Fe2p_{1/2}$ of Fe^{3+} ions in octahedral sites, and the peaks situated at 712.72 and 718.68 eV are correspond to $Fe2p_{3/2}$ and $Fe2p_{1/2}$ of Fe^{3+} ions in tetrahedral sites. These two series of binding energies clearly specify that the synthesized rCoF composite consumes a spinel structure [36]. For C1s XPS spectrum, it was divided into three consecutive peaks, which are displayed in Fig. 4 (d). The peaks at 284.89, 286.47, and 288.86 eV generally corresponds to C=C, C-O, and O-C=O, correspondingly. The oxygen-containing groups originate from rGO sheets and their fastening on Fe and Co ions sites. Meanwhile, the weak intensity of these bonds represents the large proportion of oxygen groups, that was eliminated during the conversion of GO to rGO. O1s spectrum's peak located at 530 eV represents the oxygen ions involved in the crystal lattice of Co-O-Fe cobalt ferrite, and the binding energy peaks at 531 and 532.7 eV, can be attribute to the oxygen double-bond to carbon (C=O), oxygen single-bond to carbon (C–O) respectively, are displayed in Fig. 4 (e). All the above XPS analysis was a strong proof of the elements contained in the materials which represents the successful preparation of the materials.

3.4. Brunauer-Emmett-Teller (BET)

In electrochemical studies, surface area and pore size distribution are the most important factors for electron transport [37]. The N_2- adsorption-desorption measurements for the as-synthesised CoF, rCoF-25, and rCoF-50 nanocomposites are showed in fig. 5(a, b and c). All the samples show a type IV isotherm with a hysteresis loop confirming the existence of a mesoporous structure. According to the BET analysis, the total surface area and pore diameter of the rCoF-50 nanocomposite achieved 265.1 m^2g^{-1} and 5.3 nm, which were higher than those of CoF (194.6 m^2g^{-1}) and rCoF-25 (247,8 m^2g^{-1}) samples. The interconnected systems between CoF and rGO provide a large surface area, thus increasing the charge transport path of the ions. The BJH pore size distributions of the materials are exposed in the insert, Fig. 5 (a, b and c). The adsorption division of the isotherm revealed that the common of the pore diameter was spread in a relatively high-intensity peak between 2 and 10 nm. Based on the BJH model rCoF-50 nanocomposite exhibits a pore volume of 0.682 cm^3g^{-1} which is greater than that of CoF (0.321 cm^3g^{-1}) and rCoF-25 (0.576 cm^3g^{-1}). The mesoporous scenery of the nanocomposites through pore-diameters in the series of 2–50 nm could develop the electrochemical routine and better electrolyte diffusion over nanochannels [38]. As a result, it is anticipated that rCoF nanocomposite is expected to offer additional active sites than bare CoF samples in the electrochemical method. Table 1 provides a summary of the specific surface area, which was determined using the adsorption-desorption isotherms.

Table 1. Shows the list of parameters obtained from BET analysis

Adsorbents	Specific Surface Area (SSA) m^2g^{-1}	Pore Diameter (nm)	Pore Volume (cm^3g^{-1})
CoF	194.6	3.3	0.321
rCoF-25	247.8	4.9	0.576
rCoF-50	265.1	5.3	0.682

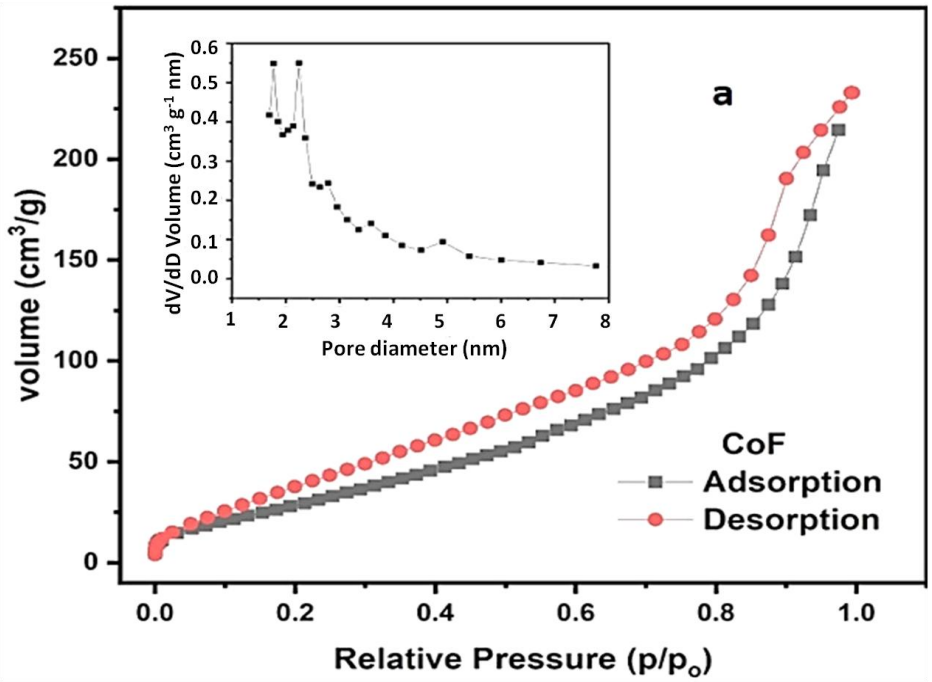

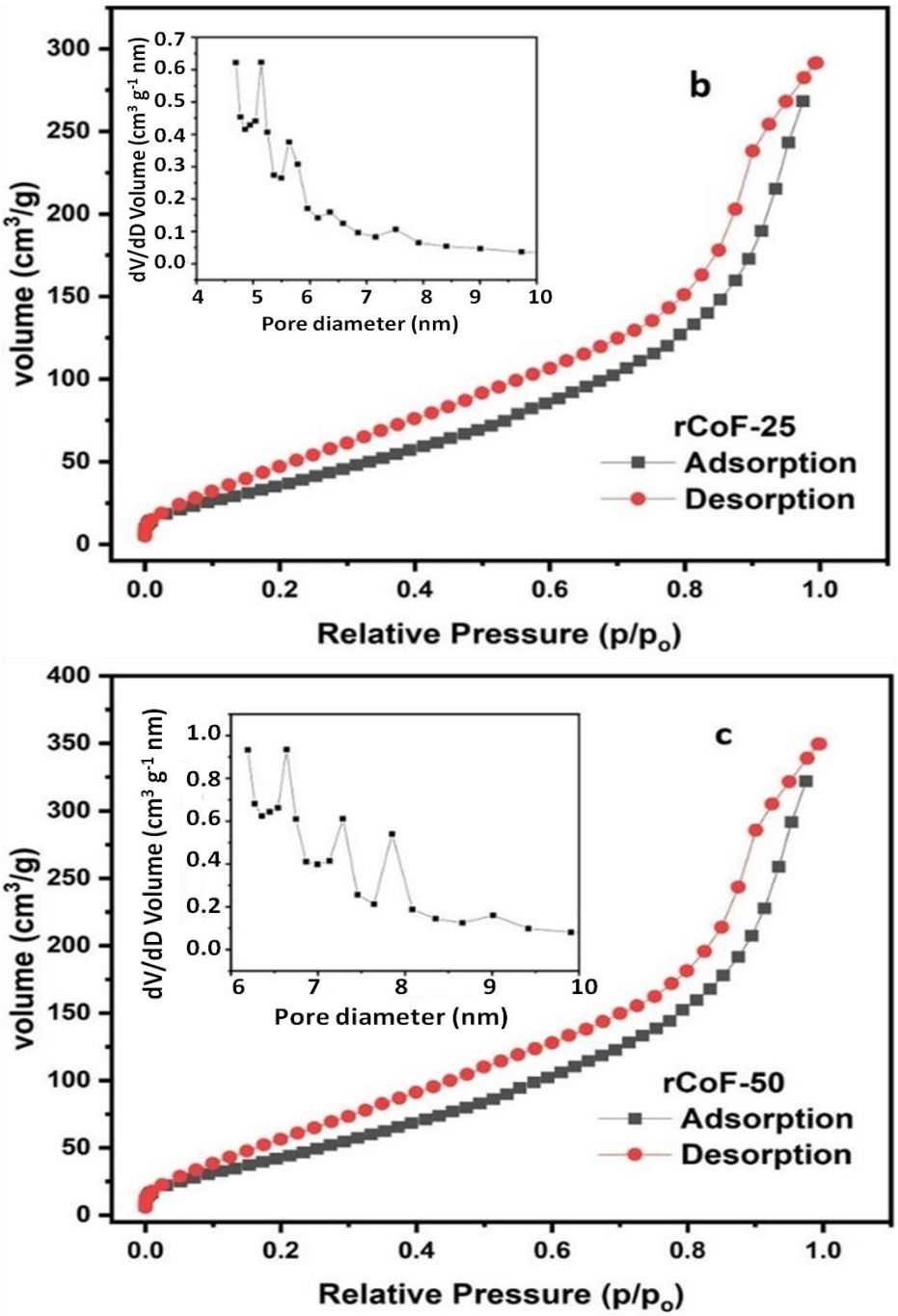

Fig. 5. (a, b and c) N_2 adsorption/desorption isotherms pore size distribution curves of CoF, rCoF-25 & rCoF-50 materials (colour online)

3.5. Electrochemical studies

3.5.1. Cyclic voltammetry (CV)

To be aware of the catalytic properties and reaction kinetics of the counter electrodes (CE) were investigated by cyclic voltammetry (CV) measurements. In this study, we examined the electrocatalytic performance of five CEs, such as rGO, Pt, CoF, rCoF-25 and rCoF-50, as given in Fig. 6. The pair of redox peaks are observed in all CEs, which signifies that iodide is oxidized to iodine (oxidation peak) conversely, iodine is reduced to iodide (reduction peak) when the potential scan direction is overturned [39].

$$I_3 + 2e^- \leftrightarrow 3I^- \text{ (Oxidation)}$$

$$3I_2 + 2e^- \leftrightarrow I_3^- \text{ (Reduction)}$$

The catalytic behaviours of the CEs were estimated by two key parameters, such as the cathodic peak density of current (J_{pc}) and the peak-to-peak division (E_{pp}) in the redox response. The value of J_{pc} is associated with rapid reduction. While, the value of E_{pp} exposes the reversibility of the redox

reaction, generally high J_{pc} and poorer E_{pp} value favoured the superior catalytic activity of the CEs [40]. According to table 2, the resulting J_{pc} value are in the subsequent runs rCoF-50<Pt<rCoF-25<rCoF<rGO, and E_{pp} value are in the overturn runs. The catalytic activity of rCoF-50 CE was found to be superior to that of Pt for its higher J_{pc} and lower E_{pp} values, which results in more triiodide (I_3^-), which is converted into iodide (I^-). It was also practical that the graphene-based electrodes manifested a high density of current and a larger enclosed redox reaction. The distribution of reduced graphene oxide is used to inhibit the aggregation of CoF, which probably increases the electrolyte-accessible surface area of the CE. Besides, rGO and CoF CE have unobvious redox peaks because of their poor catalytic performance.

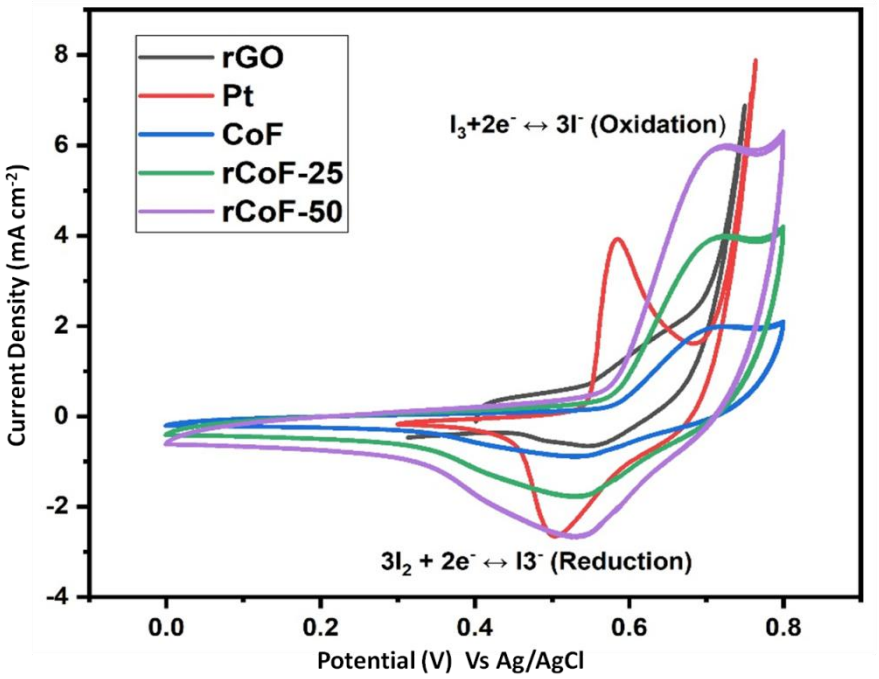

Fig. 6. CV curve of rGO, Pt, CoF, rCoF -25 & rCoF-50 (colour online)

3.5.2. Electrochemical impedance spectroscopy (EIS)

To evaluate the charge transport behaviour of the counter electrode EIS was performed. Fig. 7 illustrates a symmetric dummy cell configuration composed of CE/electrolyte/CE along with the corresponding Nyquist plot for different CE. It exhibits two distinct semicircles, each representing different resistive and capacitive elements of the system. The Ohmic resistance (Rs)**,** observed in the high frequency region, reflects the combined resistance of the electrolyte and the intrinsic resistance of the substrate**.** The charge-transfer resistance (Rct)**,** represented by the second semicircle, corresponds to the resistance to heterogeneous electron transfer occurring at the electrode-electrolyte interface**.** The low-frequency region signifies the dispersal impedance (Z_W) of I^-/I_3^- redox species in the electrolyte. Table 2 lists the values of R_s, R_{ct} and Z_w gained by fit the impedance spectra using an equivalent circuit. In general, the low R_s and R_{ct} values will decrease the boundary loss of charge transportation, and boost charge collection efficiency, which may also help to pick up the photovoltaic performance of the DSSCs [41]. The ideals of R_s and R_{ct} be reduced in the sequence of CoF > rGO > rCoF-25 > Pt > rCoF-50. Composite CEs presented little ideals of R_s and R_{ct}, evaluated among pristine CEs (CoF and rGO), suggesting that the redox couple within the composite electrode has a higher diffusion coefficient. The existence of CoF nanoparticles on the graphene layer and the homogenous immobilisation of CoF nanoparticles on graphene surfaces might minimise charge transfer resistance. According to the values of R_{ct} and R_s, the rCoF-50 possessed remarkable performance among the CEs, this is consistent with the findings of the CV measurements.

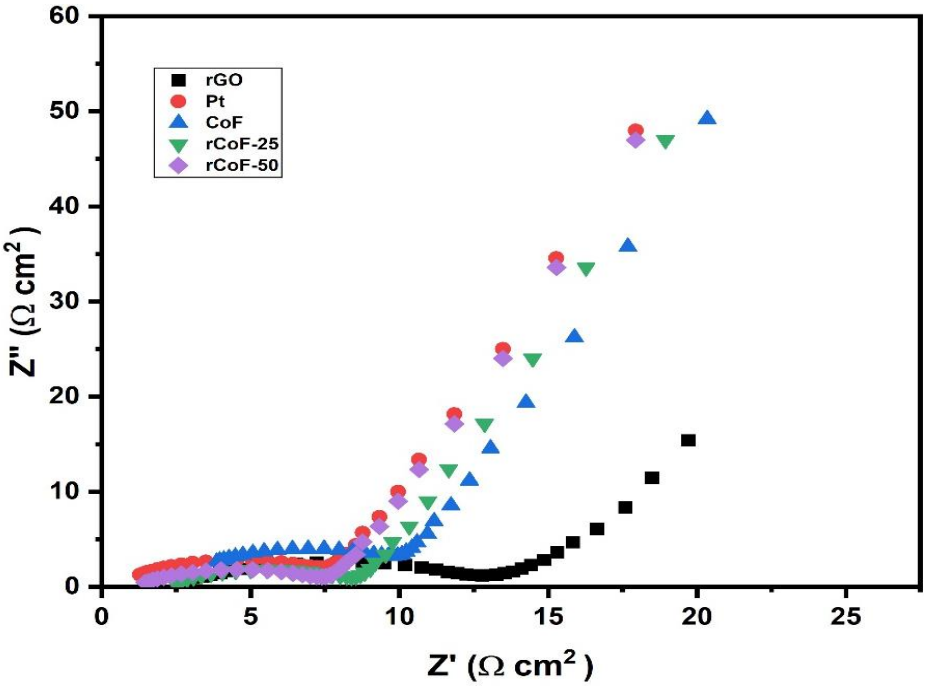

Fig. 7. Nyquist plots of made-up with rGO, Pt, CoF, rCoF -25 & rCoF-50 (colour online)

3.5.3. Tafel polarization

Tafel division curve of the imitation cells found on the CEs were also assessed and offered in Fig.8. In the Tafel polarization, the exchange density of current (J_o) achieved from the slopes of the cathodic or anodic curves replicates the electrocatalytic capacity of the CEs. Meanwhile, the partial density of current (J_{lim}) is a key factor that relates to the diffusion ability of redox couples. In this EIS investigation, the J_0 and R_{ct} value are inversely correlated. Where J_{lim} is directly proportional to the electrolyte's ion diffusion coefficient [42-43].

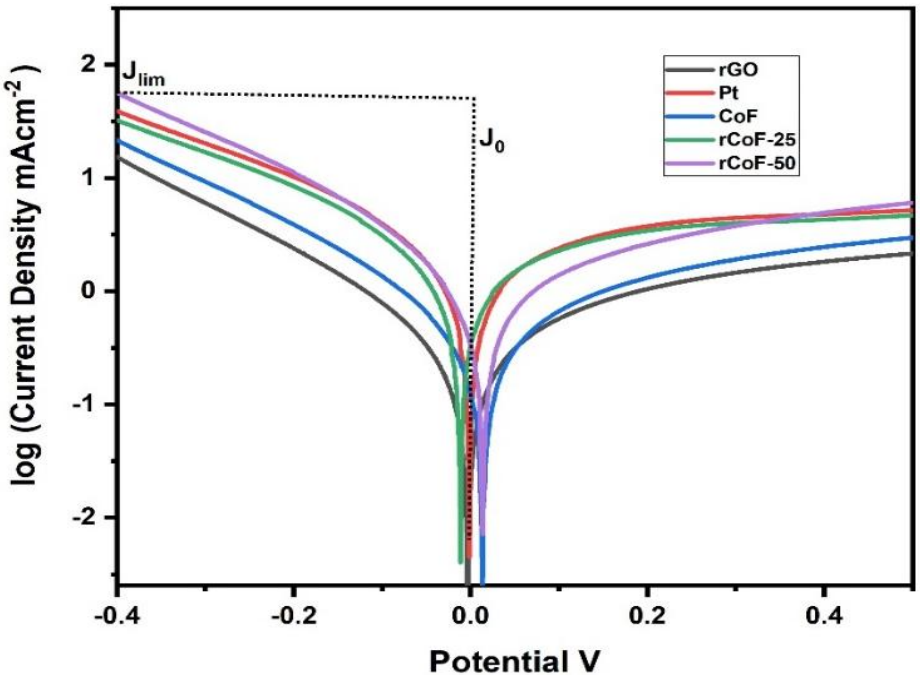

Fig. 8. Tafel polarization profile of rGO, Pt, CoF, rCoF -25 & rCoF-50 CEs (colour online)

Therefore, the counter electrode material must have higher J_0 and J_{lim} values. From the following equations, we can determine the values of J_o and J_{lim}:

$$J_o = \frac{RT}{nFR_{ct}} \quad (3)$$

$$D_{eff} = \frac{\delta}{2nFC} J_{lim} \quad (4)$$

Here, R represents the ideal gas constant, T denotes the room temperature, n is the number of electrons involved in the reduction of I_3^-, and F refers to the Faraday constant. Additionally, δ specifies the distance between the electrodes, CCC indicates the concentration of I_3^- ions, R_{ct} corresponds to the charge transfer resistance derived from the EIS analysis. In addition, Table 2 includes a summary of the calculated J_0 and J_{lim} values for the CEs. In contrast to platinized CEs, rCoF-50 CE showed a superior electro catalytic activity toward tri-iodide reduction, as evidenced by higher values of J_o and $J_{lim.}$ The superior values of J_o and J_{lim} are able to be credited to the synergistic cause of CoF and reduced graphene oxide, which might result in rapid charge transfer at the electrode/electrolyte interface. Other CEs show much lower values of J_0 and J_{lim} due to the lack of conductive channels in the structure, which results in low electron transfer abilities.

Table 2. CV, EIS and Tafel factor of the CE with the electrolyte of I_3^-/I^- redox couple

CEs	J_{red}	E_{pp} (mA cm^{-2})	R_s (Ω)	R_{ct} (Ω)	Z_w (Ω)	log J_o (mA cm^{-2})	log J_{lim} (mA cm^{-2})
rGO	0.7	1.45	8.9	2.15	0.89	0.133	1.17
Pt	2.9	1.24	7.4	1.17	0.32	0.441	1.57
CoF	0.9	1.32	8.6	2.65	0.8	0.312	1.26
rCoF-25	2.3	1.28	7.1	1.43	0.34	0.431	1.49
rCoF-50	3.2	1.17	6.8	0.80	0.24	0.654	1.81

3.6. Photovoltaic studies

The photovoltaic performance of the CEs was evaluated, and their photocurrent density versus voltage (I−V) curves is illustrated in Fig. 9. Key photovoltaic parameters, including open-circuit voltage (V_{oc}), short-circuit current density (J_{sc}), fill factor (FF), and photo-conversion efficiency (η) were analyzed and are briefed in Table 3. The photovoltaic characteristics of the DSSC mechanism made from rCoF-50 CE demonstrated a photo conversion effectiveness of 9.05% which was greater than to facilitate of Pt CE at 8.53%. The conversion efficiency of the rCoF-25 CE was 7.6%, which is very similar to the Pt CEs. The high value of J_{sc} (18.21 mA/cm^2) in rCoF-50 CE is due to the efficient reduction of I_3^-/I^- ions, fast dye regeneration at the photo anode and high photocurrent [44]. Noticeably, the V_{oc} and FF values of the DSSC based on the rCoF-25 (V_{oc}=0.68, FF= 0.69) and Pt (V_{oc}=0.69, FF=0.69) CEs are almost the same, but the value of J_{sc} was minor than that of the DSSC supported on the Pt CE. As a outcome, the total presentation of the DSSC supported on the rCoF-25 CE is approximately 90% better than with the aim of the DSSC with a conventional Pt CE. Moreover, the addition of rGO to the CoF structure is in favour of producing high electronic conductivity, and larger contact areas with an electrolyte. Moreover, DSSC cells with rGO and CoF-based CEs show relatively low efficiencies (η =5.2 and 5.7 %) which may be due to the lesser electro catalytic ability of triiodide reduction.

Finally, it is important to note that the performance of DSSC with rCoF-50 CE compares favourably to that of DSSC with straight Pt CE. Therefore, the novel rCoF-50 nanocomposite may serve as a viable choice to replace the conventional and costly Pt CE in DSSC. Table 4 shows the conversion efficiency of the prepared material and it was compared with some of the earlier reports.

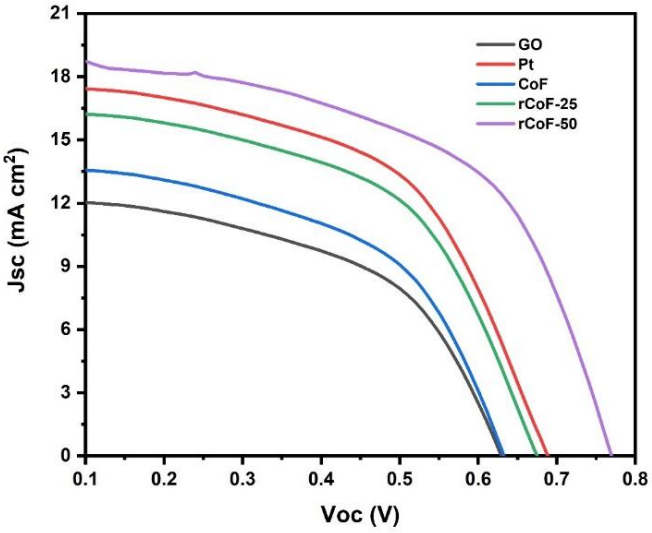

Fig. 9. Photocurrent density-voltage (I-V) profiles of DSSC support on rGO, Pt, CoF, rCoF -25& rCoF-50 CEs (colour online)

Table 3. Photovoltaic factors of fabricated DSSCs among diverse CEs

CEs	J_{sc} (mA/cm^2)	V_{oc} (V)	(FF)	η (%)
rGO	12.04	0.645	0.61	4.73
Pt	17.95	0.69	0.69	8.5
CoF	13.60	0.63	0.65	5.7
rCoF-25	16.29	0.68	0.69	7.6
rCoF-50	18.21	0.71	0.70	9.05

Table 4. Similarity of photovoltaic factors of some various CE in DSSCs

CEs	Voc (V)	J_{SC} mAcm^{-2}	FF	η(%)	Ref.
SnO_2@rGO	0.72	13.55	58.97	5.76	18
CoNiS/GN	0.75	18.33	0.68	9.42	20
r-NiF-25	0.689	17.63	0.69	8.41	29
$CoFe_2O_4$/GN	0.771	22.08	0.53	9.04	50
rCoF-50	0.71	18.21	0.70	9.05	This work

3.7. Supercapacitor studies

As a vision for the future energy crisis, the usage of solar cells in combination with supercapacitor devices was assessed via CV, GCD and EIS in 1M Na_2SO_4 electrolyte using a two-electrode configuration [45-48]. The asymmetric supercapacitor was gathered with the positive electrode as rCoF-50 and the negative electrode as activated carbon (AC), respectively. Fig. 10 (a) displays the CV profile of rCoF-50 electrodes that were examined at a sweep speed of 5 mV s^{-1} to 100 mV s^{-1} in a potential interval of 0 to 0.8 V, respectively. The observed CV profile implies that the capacitance moves towards from the mixture of together the electric double-layer capacitance of rGO and the CoF components of pseudo capacitance. Moreover, the CV area expanded steadily as the scan rate starting 5 mVs^{-1} to 100 mV s^{-1} and retaining the same shape while sweeping at high scan rates, suggesting the rapid charge/discharge rates endowed by the hierarchical nanosheet structure and stable electrochemical responses even at 100 mV s^{-1} [49]. The good electrochemical behaviour of the rCoF-50 electrode is attributed to its fast reaction process, and extensively reduces the flow time of sodium ions at the boundary of the electrode. The aforementioned finding shows that the rCoF-50 composite can function well under high current charge-discharge cycles. The CV curves are used to derive the values of specific capacitance (C_s Fg^{-1}) using the below equation:

$$C_s = \frac{1}{mv\,(Vc-Va)} \int_{Va}^{Vb} Idv \qquad (5)$$

where, C_s (Fg^{-1}) is specified capacity, V (Vs^{-1}) is the scanning speed of the Cv curve, Vc – Va (V) symbolises the two working potential limits, I (A) is current and m is mass loading on the current collector (g). The estimates specified capacity (C_s Fg^{-1}) of the rCoF-50 electrode from CV curve was found to be 361 Fg^{-1}. To go one step additional, the galvanometric charge-discharge (GCD) of the as-synthesised electrode was assessed at various current density of 1, 2, 3, 4 and 5 Ag^{-1} correspondingly. The charge-discharge profile of the rCoF-50 electrode is illustrated in Fig. 10 (b). The expression that follows is use to estimate the values of specific capacitance from GCD profile [50]:

$$C_s = \frac{I\Delta t}{m\Delta V} \qquad (6)$$

where, C_s (Fg^{-1}) is specific capacitance of the active sample, I is the applied constant current (A), Δt is discharging time of one cycle (s), ΔV (V) is discharging potential and m represents the mass of the active electrode material (g). Based on charge-discharge profile the specified capacity of rCoF-50 electrode was estimated at 388.7, 334.2, 287.5, 251.8 and 203.9 Fg^{-1} at various density of current 1, 2, 3, 4 and 5 Ag^{-1} respectively, which was also coincided with the CV results. The high value of specified capacity could be owing to the simple diffusion of electrolytes, the accessibility of many active sites, and the uniform porous structures, which help to improve electron transportation [29]. As illustrated in fig 10 (c), the decrease in specified capacity is owing to the increase in potential fall when the current density increases. In practical applications, cyclic performance is one of the crucial factors. As shown in Fig. 10d, the longevity measurements were monitored up to 2000 cycles at a current density of 3 Ag^{-1}, and the capacitance retention reached 90.5%, demonstrating the superior cyclic stability of the rCoF-50 electrode. Due to rGO, the electrical and mechanical stability of the nanocomposites have been significantly enhanced at the same time, rGO was also acting as an elastic barrier, which decrease the volume change of the rCoF-50 electrode during the charge-discharge route. These findings show that the rCoF-50 electrode exhibits remarkable cyclic strength and excellent rate capacity. Additionally, to consider the conductivity of the electrode/electrolyte region, electrochemical impedance spectroscopy (EIS) was used as an essential parameter. Fig. 10 (e) shows the EIS Nyquist plot of the rCoF-50 electrode, and the inset diagram displays the corresponding equivalent circuit model. The plot consists of equivalent series resistance (ESR), charge transfer resistance (R_{ct}), double-layer capacity (C_{dl}), Faradaic capacity (C_p) and Warburg element (W) respectively [49]. The EIS Nyquist plot of rCoF-50 electrode reveals a single half circle in the high-frequency section and a vertical line in the low-frequency section. At high-frequencies, the interrupt along the real X- axis specifies the equivalent series resistance of the electrochemical system (R_s) which includes the combination of the electrolyte, electrode material, and interfacial resistance, respectively. At the mid frequency

region, a small half circle specifies the charge-transfer resistance (R_{ct}) of the electrode. The charge of ESR and R_{ct} of the rCoF-50 electrode was found to be 4.6 and 2.4 Ω/cm^2 respectively. This high charge storage capacity is the result of the low ESR and R_{ct} values in rCoF-50, which indicate an excellent ion responsiveness and better electronic conductivity.

Moreover, reduced graphene oxide offers fast electrode charge transfer rates and a short ion transfer path.

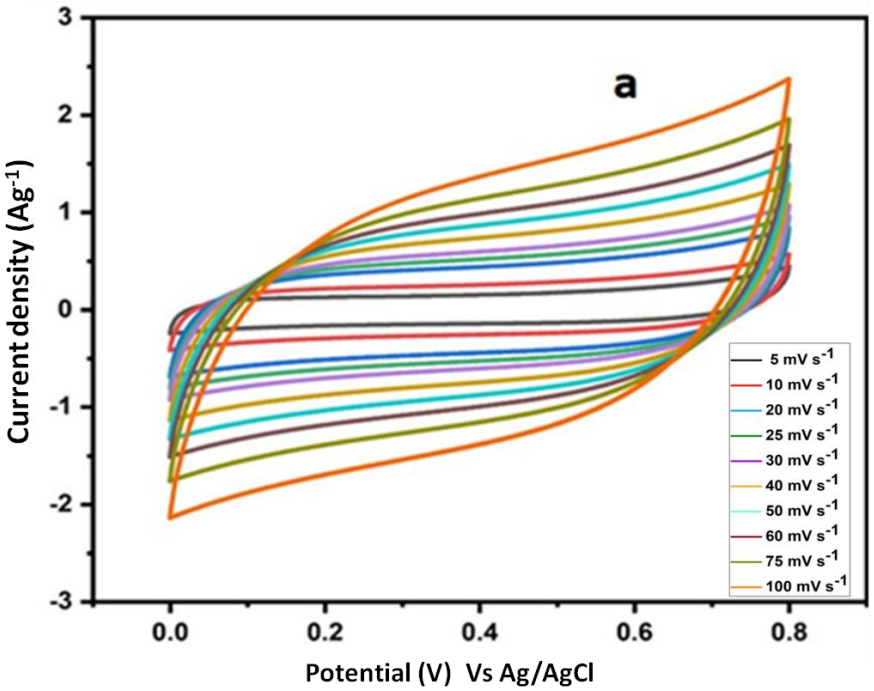

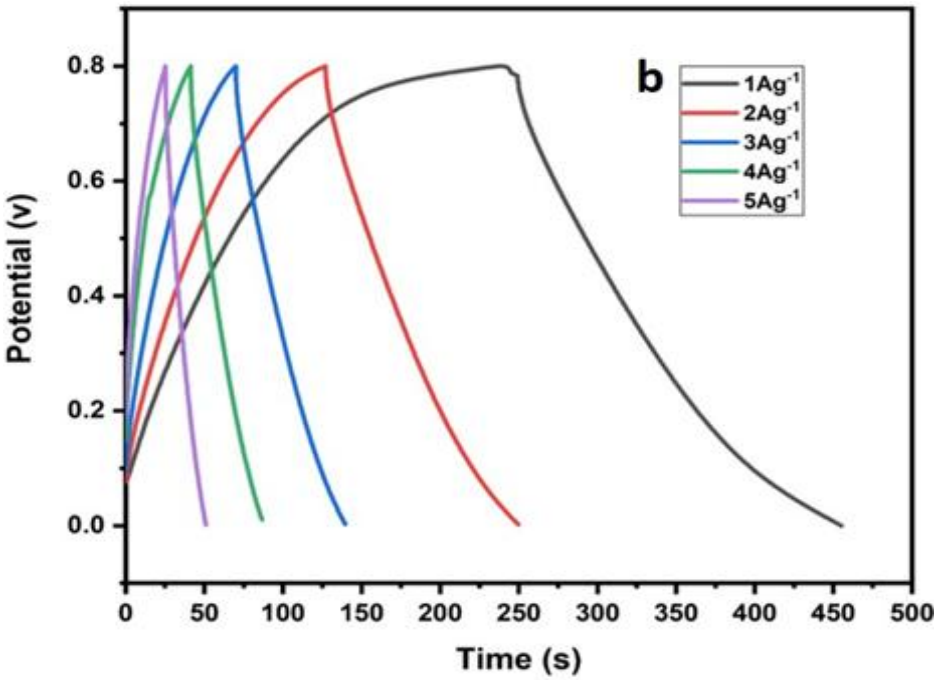

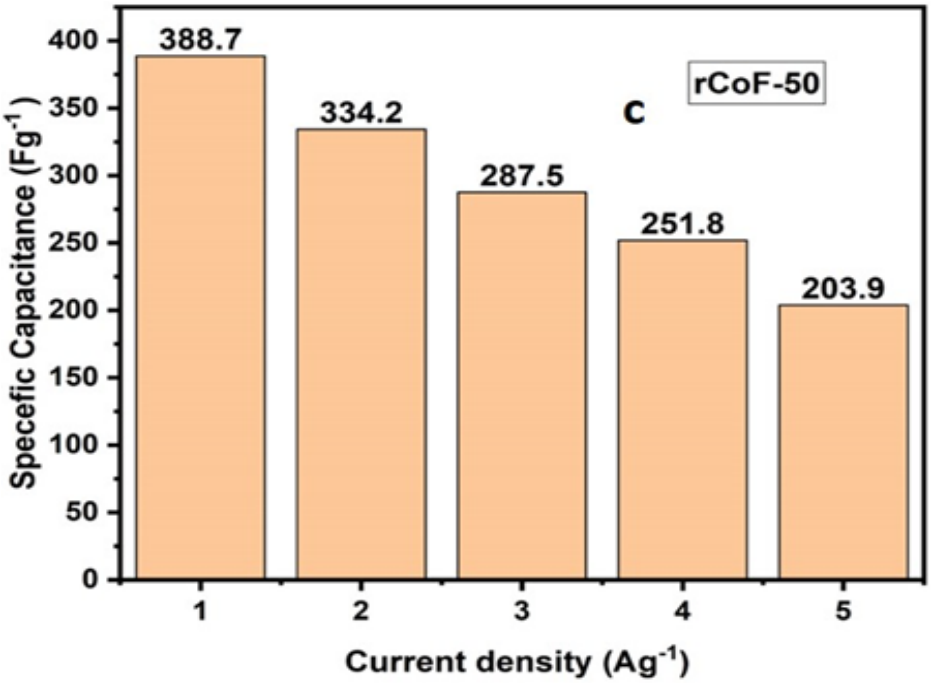
388.7
334.2
287.5
251.8
203.9
c
rCoF-50
Specefic Capacitance (Fg-1)
Current density (Ag-1)

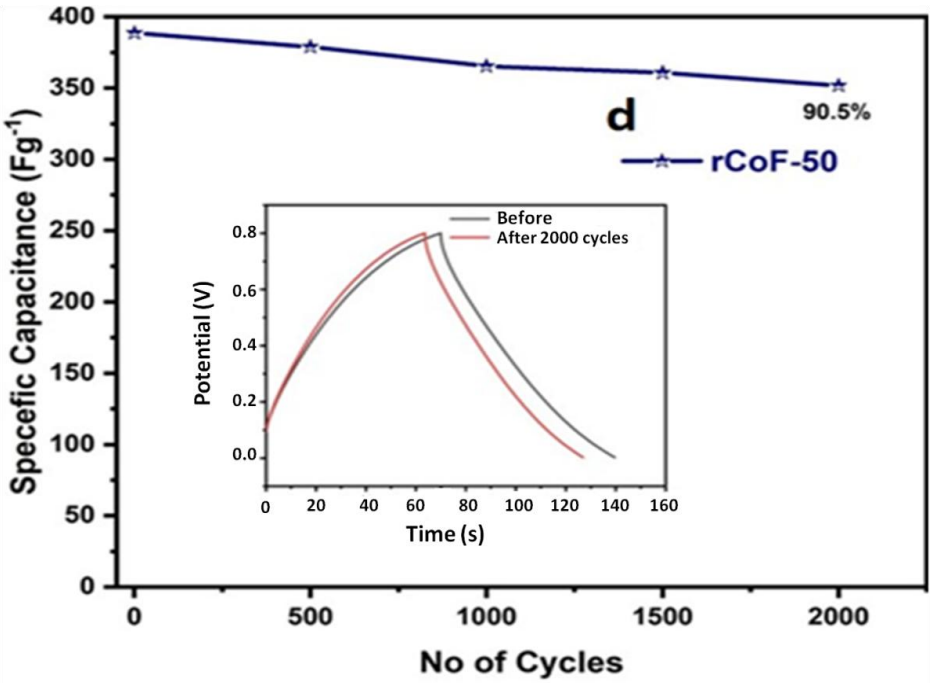
d
90.5%
rCoF-50
Before
After 2000 cycles
Potential (V)
Time (s)
Specefic Capacitance (Fg-1)
No of Cycles

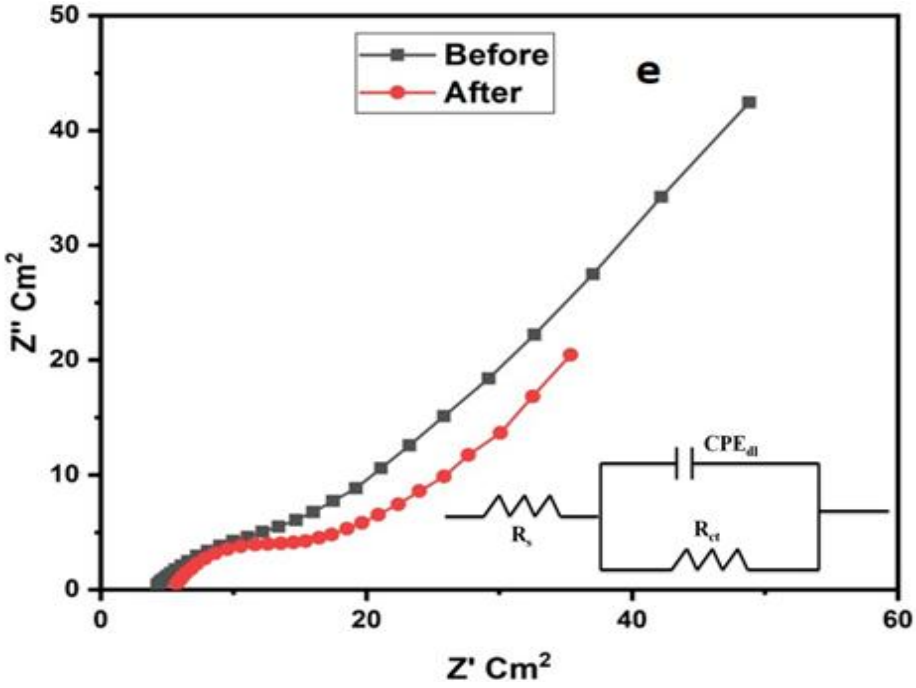

Fig. 10. (a-e) shows the CV, GCD, Capacitance histogram, Cyclic retention, and EIS plots of rCoF-50 supercapacitor electrode (colour online)

4. Conclusion

In outline, rGO/$CoFe_2O_4$ nanocomposites have been effectively prepared by one pot hydrothermal method. XRD studies confirm the formation of fine quality of the nanocomposites. From HR-TEM analysis, it is worth noticing that freely accumulated CoF nanoparticles extend on together surface of rGO sheets, demonstrating a multilayer structure. The XPS study reveals the existence of atomic orbitals such as Co2p, Fe2p, O1s, and C1s with high resolution. The observed results from electrochemical studies suggest that the rCoF-50 CE has better electrocatalytic activity towards tri-iodide reduction compared to the other CEs counting platinized CE. The photovoltaic characteristics of the DSSC device made from rCoF-50 CE manifest a photo conversion effectiveness of 9.05%, which is superior to that of Pt CE at 8.53 % respectively. The fabricated asymmetric supercapacitor with the rCoF-50 nanocomposite showed a good electrochemical property of 388.7 Fg^{-1} at a density of current is 1 Ag^{-1}, and it has achieved desirable capacity withholding of 90.5% behind 2000 charge-discharge cycles at a density of current is 3 Ag^{-1}. Over all, these outcomes suggest that rCoF-50 CE is a bright prospect for energy conversion and storage devices.

References

[1] S. J. Patil, A. C. Lokhande, J. S. Park, J. H. Kim, Y. B. Kim, B. C. Choi, S. H. Park, S. H. Jung, D. W. Lee, Journal of Industrial and Engineering Chemistry **61**, 206 (2018).
[2] J.-M. Kim, S.-W. Rhee, Electrochimica Acta **83**, 264 (2012).
[3] A. Cabrera-Tobar, E. Bullich-Massagué, M. Aragüés-Peñalba, O. Gomis-Bellmunt, Renewable and Sustainable Energy Reviews **59**, 309 (2016).
[4] S. C. Lau, H. N. Lim, T. B. Ravoof, M. H. Yaacob, D. M. Grant, R. C. MacKenzie, I. Harrison, N. M. Huang, Electrochimica Acta **238**, 178 (2017).
[5] T. Prasankumar, B. R. Wiston, C. R. Gautam, R. Ilangovan, S. P. Jose, Journal of Alloys and Compounds **757**, 466 (2018).
[6] J. Vigneshwaran, S. Abraham, B. Muniyandi, T. Prasankumar, J.-T. Li, S. P. Jose, Surfaces and Interfaces **27**, 101572 (2021).
[7] T. Prasankumar, D.-J. Kang, M. Kim, H.-T. Lim, International Journal of Elecrochemical Science **18**(10), 100315 (2023)
[8] J. Vigneshwaran, T. Prasankumar, M. N. M. Ansari, H.-T. Lim, B. Yuliarto, S. P. Jose, Journal of Materials Science **59**, 10953 (2024).
[9] S. P. Jose, C. S. Tiwary, S. Kosolwattana, P. Raghavan, L. D. Machado, C. Gautam, T. Prasankumar, J. Joyner, S. Ozden, D. S. Galvao, P. M. Ajayan, RSC Advances **6**, 93384 (2016).
[10] H. W. Chen, C. Y. Hsu, J. G. Chen, K. M. Lee, C. C. Wang, K. C. Huang, K. C. Ho, Journal of Power Sources **195**(18), 6225 (2010).
[11] R. B. Schainker, IEEE Power Engineering Society General Meeting, 2309 (2024).
[12] A. Ali, S. Khurram, U. R. Faiz, M. S. Syed, K. Muhammad, M. Muhammad, R. S. Rizwan, ACS Applied Materials and Interfaces **38**, 25353 (2016).
[13] F. Hao, L. Hong, L. Yizhu, W. Ning, L. Wendi, L. Jianbao, ACS Applied Materials and Interfaces **10**,

3916 (2011).
[14] A. Rani, C. Kyungwha, K. Jeong, J. K. Sung, H. J. Yoon, J. J. Yu, N. Q. Li, Y. Minji, H. P. Jong, H. K. Dong, ACS Applied Materials and Interfaces **18**, 11488 (2016).
[15] P. Sudhagar, S. Nagarajan, Y.-G. Lee, D. Song, T. Son, W. Cho, H. Miyoung, L. Kyoungjun, W. Jongok, S. K. Yong, ACS Applied Materials and Interfaces **6**, 1838 (2011).
[16] W. Yan, Y. Zhenrong, B. Weiyong, Y. Ruizhi, Carbon **92**, 74 (2015).
[17] J. Song, G. R. Li, X. Kai, B. Lei, X. P. Gao, Journal of Materials Chemistry A **26**, 10041 (2014).
[18] F. Du, Y. Bo, Z. Xueqin, L. Guang, Materials Letters **158**, 424 (2015).
[19] K. Xiong, L. Guang, J. Cheng, J. Shaowei, Materials Letters **164**, 609 (2016).
[20] V. Murugadoss, P. Pratheep, Y. Chao, G. Zhanhu, A. Subramania, Electrochimica Acta **312**, 157 (2019).
[21] Y. Wang, G. Yanjun, C. Wentao, L. Qing, L. Wenli, X. Peng, C. Dongliang, Y. Xiong, H. Meng, Applied Surface Science **452**, 232 (2018).
[22] J. Xia, W. Qi, C. Miaomiao, L. Wenwen, L. Jie, C. Jitang, W. Hai, F. Suhua, Electrochimica Acta **307**, 422 (2019).
[23] J. Yang, N. Yudi, H. Jie, L. Linchun, Q. Xing, Electrochimica Acta **330**, 135333 (2020).
[24] S. Wang, W. Xiaoyan, X. Ying, J. Wenchao, W. Xiuwen, J. Yi, Z. Wei, P. Kai, Journal of Alloys and Compounds **803**, 216 (2019).
[25] C. T. Altaf, O. Coskun, A. Kumtepe, A. M. Rostas, I. Iatsunskyi, E. Coy, E. Erdem, M. Sankir, N. D. Sankir, Scientific Reports **12**, 11487 (2022)
[26] P. S. Chauhan, M. Parekh, S. Sahoo, S. Kumar, A. D. Mashapatra, P. Sharma, V. Panwar, A. M. Rao, A. Misra, Journal of Materials Chemistry A **12**, 22725 (2024).
[27] H. C. Prakash, M. Sathish Kumar, T.-W. Lin, S. K. Batabyal, Electrochimica Acta **469**, 143229 (2023).
[28] P. C. Santhosh, S. Jayakumar, M. M. Mohideen, A. V. Radhamani, Materials Research Bulletin **174**, 112722 (2024).
[29] S. V. Anto Feradrick, S. B. Bernadsha, J. F. Britto, M. Victor Antony Raj, J. Madhavan, Diamond and Related Materials **130**, 109406 (2022).
[30] D. Nathan, T. Muthu Gnana, S. Jacob Melvin, Journal of Alloys and Compounds **700**, 67 (2017).
[31] L. Yue, Z. Shuaiguo, Z. Hanqing, F. Yu, W. Miao, A. Lulu, Z. Xiaodan, M. Jie, Solid State Ionics **329**, 15 (2019).
[32] M. B. Askari, S. Parisa, International Journal of Hydrogen Energy **51**, 27482 (2020).
[33] X. Xu, Z. Wei, Z. Xi, D. Jin, X. Zhigang, S. Yuan, W. Tingting, D. Youwei, Journal of Colloid Interface Science **543**, 147 (2019).
[34] D. Zhang, G. Shiyao, Z. Jiwei, W. Jingruo, S. Wenna, W. Kunjie, X. Xu, Y. Biao, M. Xianxin, Journal of Power Sources **514**, 230590 (2021).
[35] Y. Cao, F. Naeim, M. Nasser, V. Y. Alexei, N. A. Majid, A. Arash, Ceramics International **47**, 12244 (2021).
[36] V. Mahdikhah, S. Saadatkia, S. Sheibani, A. Ataie, Optical Materials **108**, 110193 (2020).
[37] V. M. Vimuna, A. R. Athira, K. V. Dinesh Babu, T. S. Xavier, Diamond and Related Materials **110**, 108129 (2020).
[38] J. Song, L. Wenting, X. Jianjiao, W. Wenbo, S. Kun, C. Xiaoshuang, Y. Guangming, Applied Surface Science **568**, 150915 (2021).
[39] J.-D. Peng, Y.-T. Wu, M.-H. Yeh, F.-Y. Kuo, R. Vittal, K.-C. Ho, ACS Applied Materials and Interfaces **12**, 44597 (2020).
[40] L. Chen, C. X. Guo, Z. Qiaoming, L. Yanlian, X. Jiale, E. Shujing, G. Guanhong, S. Qunliang, M.-L. Chang, ACS Applied Materials and Interfaces **5**, 2047 (2013).
[41] M. Song, A. Sadia, M. S. Akhtar, H.-K. Seo, H.-S. Shin, Materials Research Bulletin **48**, 4538 (2013).
[42] Y. Liao, P. Kai, W. Lei, P. Qingjiang, Z. Wei, M. Xiaohuan, J. Baojiang, ACS Applied Materials and Interfaces **5**, 3663 (2013).
[43] T. Peng, S. Weiwei, H. Chengliang, Y. Wenjing, S. Bobby, D. Zhigao, G. Shishang, X.-Z. Zha, ACS Applied Materials and Interfaces **6**, 14 (2014).
[44] R. J. Mathew, C.-P. Lee, C.-A. Tseng, C. Pradyumna Kumar, Y.-J. Huang, H.-T. Chen, K.-C. Ho, A. Aswin Kumar, C.-H. Lee, Y.-T. Chen, ACS Applied Materials and Interfaces **12**, 34815 (2020).
[45] S. K. Vijaya, R. Kalai Selvan, Electrochimica Acta **213**, 469 (2016).
[46] X. Zhang, Z. Mingchang, O. Tian, C. Ye, Y. Jun, Z. Kai, Y. Ke, W. Guiling, C. Kui, C. Dianxue, Chemical Engineering Journal **360**, 171 (2019).
[47] G. Nabi, R. Waseem, A. K. Muhammad, A. Thamer, R. Muhammad, T. Muhammad Bilal, H. Sajad, Journal of Energy Storage **29**, 101452 (2020).
[48] K. Song, Y. Rui, W. Xin, Z. Bin, W. Jun, C. Xiaoshuang, Applied Surface Science **533**, 147433 (2020).
[49] S. Lee, J.-S. Kang, K.-T. Leung, W. Lee, D. Kim, S. Han, W. Yoo, H.-J. Yoon, N. Kyusuk, S. Youngku, Journal of Industrial and Engineering Chemistry **43**, 69 (2016).
[50] B. Pang, S. Lin, Y. Shi, Y. Wang, Y. Chen, S. Ma, J. Feng, C. Zhang, L. Yu, L. Dong, Electrochimica Acta **297**, 70 (2019).

*Corresponding author: drkarthigeyanka@veltech.edu.in; manikandan.e@vit.ac.in